Journal of
Marine Science and Engineering

Article

Effect of Flow Rate on Regular Patterns of Pressure Load Distribution on Helico-Axial Pump Impeller Blade Surface

Zongliu Huang , Guangtai Shi * and Haigang Wen

Key Laboratory of Fluid and Power Machinery, Ministry of Education, Xihua University, Chengdu 610039, China
* Correspondence: sgtaixh@126.com

Abstract: In this paper, the *k*-*ω* SST (Shear Stress Transport) turbulence model is employed to study the effect of flow rate on regular patterns of pressure load distribution characteristics on the helico-axial pump impeller blade surface. The results show that all the curves of pressure load distribution of helico-axial pump impeller blade surface at different blade heights under different flow rates show a similar trend of increasing first and decreasing then. At the impeller blade inlet area, with the increase of flow rate, the range of negative blade pressure load in this area gradually increases. When the pump runs under small flow rate conditions, within the range of relative position from 0 to 0.2 of the hub, the work capacity of the hub is obviously stronger than that of other areas of the impeller, while within the range of relative position from 0.2 to 1, the work capacity from hub to rim gradually enhances. With the increase in flow rate, the area with a strong work capacity of the hub gradually expands while the area with a strong work capacity of the rim gradually narrows. The research results can provide a theoretical reference for the optimization design of pump supercharging performance.

Keywords: helico-axial pump; pressure load; impeller blade; flow rate

check for updates

Citation: Huang, Z.; Shi, G.; Wen, H. Effect of Flow Rate on Regular Patterns of Pressure Load Distribution on Helico-Axial Pump Impeller Blade Surface. *J. Mar. Sci. Eng.* **2023**, *11*, 13. https://doi.org/10.3390/jmse11010013

Academic Editor: Kamal Djidjeli

Received: 11 November 2022
Revised: 4 December 2022
Accepted: 18 December 2022
Published: 21 December 2022

1. Introduction

The helico-axial pump is mainly used for transporting crude oil, and it is a type of excellent fluid machinery [1–3]. The helico-axial pump performance directly determines the efficiency of transporting medium. Though the helico-axial pump can transport the gas-liquid multiphase medium with a large gas volume fraction [4,5], its operation efficiency is relatively low, which mainly owes to the relatively worse work capacity of the helico-axial pump impeller blade [6,7].

Now, the research on helico-axial pumps mainly focuses on internal flow mechanism, hydraulic performance, stability and other aspects. Suh et al. [8] analyzed the internal flow mechanism of a multiphase flow blade pump after a numerical optimization of both the impeller and diffuser of a multiphase pump. Shi et al. [9] studied the effect of inlet gas void fraction on the flow characteristics in the tip clearance combined the numerical and experimental methods. Based on the Oseen vortex theory, Liu et al. [10] proposed a method to optimize the performance of multi-stage multiphase by a theoretical method. Kim et al. [11] used a commercial computational fluid dynamics code and a response method in optimization to design a multiphase pump impeller and improve its performance. Xu et al. [12] found that the design of a splitter blade can significantly reduce pressure fluctuation and improve the stability and safety of a multiphase pump impeller operation by studying and experimenting with the transient pressure characteristics. Zhang et al. [13,14] mainly carried out the visualization test on a multiphase pump to investigate the liquid–gas flow pattern and its influencing factors like flow rate, rotation speed and gas proportion. Liu et al. [15] carried out the optimization design of the inlet and outlet design angle of the impellers and other factors by the orthogonal design method. Zhang et al. [16] studied the internal flow characteristics of slug flow in a helico-axial multiphase pump with different in let gas void fractions and found that affected by the flow from the slug, the flow pattern in the helico-axial multiphase pump changes sharply and resulting in severe fluctuations. Suh [17] established a numerical analysis method which was used commercial CFD packages to evaluate the multiphase flow with high reliability and proposed a numerical method to investigate the effect of different GVFs on the flow characteristics. Liu et al. [3] provided a dynamic mode and applied it to investigate the gas–liquid flow field in a three-stage helico-axial multiphase pump. Cao et al. [18] proposed a mathematical model for describing the pressure distribution inside the working chamber of a multiphase pump. Moreover, a large number of other relevant significant studies about multiphase pumps have been carried out [19–23].

At the same time, there have been many reports on the research of the work capacity of many kinds of pumps. Li et al. [24] investigated the effect of the blade loading distribution on the head, radial force and pressure pulsation of a low specific-speed centrifugal pump with cylindrical impeller blades. Shi et al. [25] investigated pressure load distribution on helico-axial pump blades under different gas volume fraction conditions. Zhang et al. [26] studied the unsteady hydrodynamic forces on a diffuser pump impeller excited by the interaction between the impeller and the vaned diffuser with the same number of vanes as the impeller by experimental and computational methods. Aimed at studying the influence of impeller rear rim radius on the axial force and pump hydraulic performance, Zhou et al. [27] investigated a centrifugal pump with different impeller rear rim radii under multi-conditions numerically and experimentally. Li et al. [28] adopted a numerical method to investigate the hydraulic force on the impeller of a model reversible pump turbine quantitatively. Zhu et al. [29] investigated the influence of leading-edge cavitation on impeller blade axial force in the pump mode of a reversible pump-turbine. Kang et al. [30] studied the operational stability of an impeller pump; the numerical method considered the dynamic influence of fluid flow, temperature and structure and found that pressure distributions remain similar at the flow rate inspected. Zhou et al. [31] researched the fluid-induced force of a centrifugal pump impeller under eccentric assembly conditions with compound whirling based on the numerical method.

It can be known from the summary of the aforesaid literature that there are few reports within the literature on the research on the work capacity of the helico-axial pump. Referring to relevant research methods, the regular patterns of pressure load distribution of the helico-axial pump impeller blade surface are studied in this paper. Through the present research, the work capacity of the pump impeller can be grasped, providing a theoretical reference for further optimization design of the pump.

2. Prototype Pump

A helico-axial multiphase pump, which was researched and developed independently by the authors, is selected as the research object in the present study [32]. Table 1 shows the main parameters of the selected helico-axial pump. Figure 1 shows the prototype helico-axial multiphase pump, which is mainly composed of the following parts, i.e., flow parts, axial force balance device, cooling system, sealing system, bearing support mode and structures. The helico-axial pump has a single compression cell, and the compression cell is constituted of a rotating impeller and a static diffuser.

Table 1. Major parameters of the helico-axial pump.

Parameters	Value	Unit
Design volume flow rate	90	m^3/h
Design rotational speed	3600	r/min
Number of impeller blade	3	-
Number of diffuser blade	11	-
Outer diameter of impeller	161	mm
Outer diameter of diffuser	161	mm

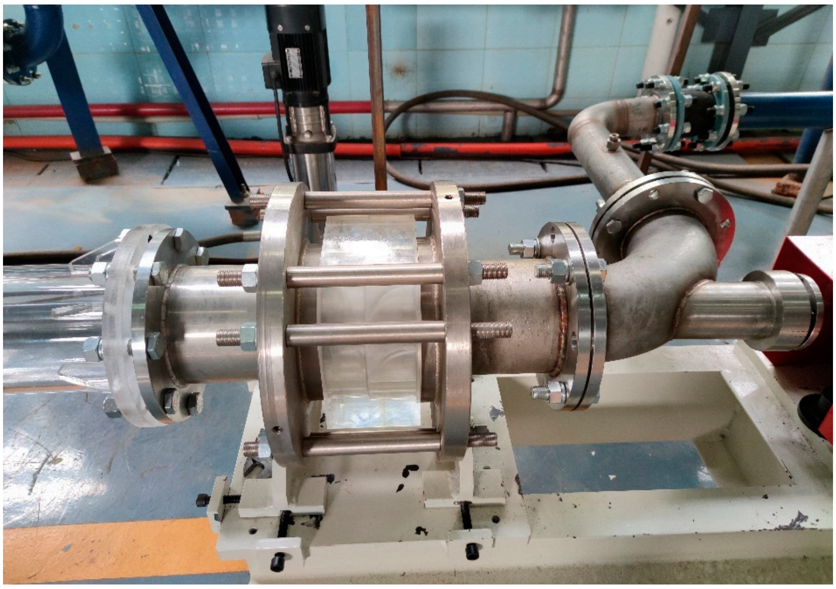

Figure 1. Prototype of the helico-axial pump.

3. Numerical Methods

3.1. Governing Equations

The Reynolds averaged RANS (Navier–Stokes equations) combined with the k-ω two-equations turbulence model based on the SST (Shear Stress Transport) model are adopted as the governing equations in the present study. The turbulence model takes the transmission of turbulent shear stress into account, which can predict the flow separation amount under negative pressure gradient more precisely so that the model owns a wider scope of application and more advantages compared to other turbulence models [3,4,33], and the obtained computing results are more reliable. The RANS equations are Equations (1) and (2).

$$\frac{\partial \overline{u_i}}{\partial x_i} = 0 \tag{1}$$

$$\frac{\partial \overline{u_i}}{\partial t} + \overline{u_j}\frac{\partial \overline{u_i}}{\partial x_j} = -\frac{1}{\rho}\frac{\partial p}{\partial x_i} + \frac{\partial}{\partial x_j}\left(\nu\frac{\partial \overline{u_i}}{\partial x_j} - \overline{u'_i u'_j}\right) \tag{2}$$

where i, j = 1, 2, 3, t is time, $\overline{u_i}$ is the averaged component of velocity, p denotes the pressure, ρ is the density of fluid, ν is the kinematic viscosity, $u_i{}'$ and $\overline{u'_i u'_j}$ denote the fluctuating component of flow velocity and Reynolds stress tensor, respectively. The Reynolds stress tensor is calculated based on the Boussinesq hypothesis equation [34], i.e.,

$$\overline{u'_i u'_j} = -\nu_t\left(\frac{\partial \overline{u_i}}{\partial x_j} + \frac{\partial \overline{u_j}}{\partial x_i}\right) + \frac{2}{3}k\delta_{ij} \tag{3}$$

where ν_t is the eddy viscosity, k is the turbulent kinetic energy, δ_{ij} is the Kronecker symbol. The turbulent kinetic energy k and the specific dissipation rate ω are solved by Equations (4) and (5).

$$\frac{\partial(\rho k)}{\partial t} + \frac{\partial(\rho \overline{u_i} k)}{\partial x_i} = P_k - \beta^* \rho k \omega + \frac{\partial}{\partial x_i}\left[(\rho\nu + \sigma_k \rho \nu_t)\frac{\partial k}{\partial x_i}\right] \tag{4}$$

$$\begin{aligned} \frac{\partial(\rho\omega)}{\partial t} + \frac{\partial(\rho\overline{u_i}\omega)}{\partial x_i} &= \left[\tfrac{5}{9}F_1 + 0.44(1-F_1)\right]\frac{P_k}{\nu_t} - \beta\rho\omega^2 \\ &+ \frac{\partial}{\partial x_i}\left[(\rho\nu + \sigma_\omega \rho \nu_t)\frac{\partial \omega}{\partial x_i}\right] + 2(1-F_1)\frac{\rho\sigma_{\omega 2}}{\omega}\frac{\partial k}{\partial x_i}\frac{\partial \omega}{\partial x_i} \end{aligned} \tag{5}$$

The eddy viscosity is solved by Equation (6).

$$\nu_t = \frac{\alpha_1 k}{\max\left(\alpha_1 \omega, \sqrt{2S_{ij}S_{ij}}F_2\right)} \tag{6}$$

All the above equations make up the governing equations in the present study. A more detailed description of the equations and parameters can be found in reference [35].

3.2. Model of Helico-Axial Pump

In order to make the inlet and outlet flow to be more fully developed, extensions are set at the inlet and outlet of the helico-axial pump pressurization unit. The computation domain model is composed of four parts, i.e., inlet extension (inlet pipe), impeller, diffuser and outlet extension (outlet pipe). The integrated BladeGen software, which is a professional modeling software for turbomachinery in ANSYS Workbench, is adopted to model the helico-axial pump impeller and diffuser. The final computation models are shown in Figure 2.

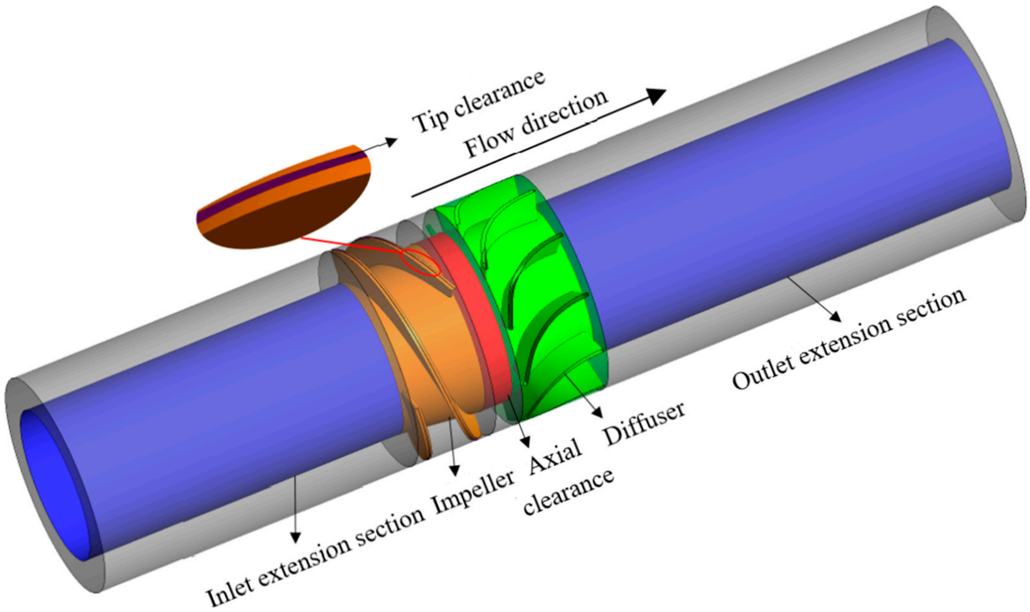

Figure 2. Computational domain.

3.3. Mesh Arrangement and Mesh Independence Validation

Through three-dimensional modeling software, in this paper, the blade profile of the impeller and diffuser and the curves of the rim and hub of the helico-axial pump are extracted from the established three-dimensional model. The control points of each profile are obtained in Bladegen software, and then the control points are introduced into Turbogrid software to carry out the structural grid division of a single passage in impeller and guide vane areas. Then, the single passage is rotated into the whole passage for setting. It is better to import the inlet and outlet extensions of the computational flow domain for hexahedral structural grid division. The near-wall meshes are refined to capture the complex flow field in the boundary layer and ensure the value of y+ in the simulation within 30.

In the numerical simulation, the quality and the number of cells can affect the accuracy and the cost of computing time directly. In this paper, four groups of grids were selected for independent verification under the same conditions. Table 2 shows the results of the relative head under different grid groups. It can be seen from Table 2 that the relative head of the pump gradually tends to stabilize with the increase in the number of grids. When the number of grids is larger than the third group, the change values of the pump head are small, and the influence of the grid number on the calculation can be ignored. Considering the computing resources and accuracy, the grid number of the computing domain is finally selected as 4.26 million. The structural grids of the computational domain are finally obtained, as shown in Figure 3.

Table 2. Mesh independence verification.

	Group 1	Group 2	Group 3	Group 4
number of grids in inlet extension (10^6)	0.51	0.51	0.51	0.51
number of grids in impeller (10^6)	0.78	1.20	1.75	2.60
number of grids in diffuser (10^6)	0.61	0.97	1.44	2.08
number of grids in outlet extension (10^6)	0.56	0.56	0.56	0.56
number of total grids (10^6)	2.46	3.24	4.26	5.75
H/H_1	1	1.021	1.036	1.040

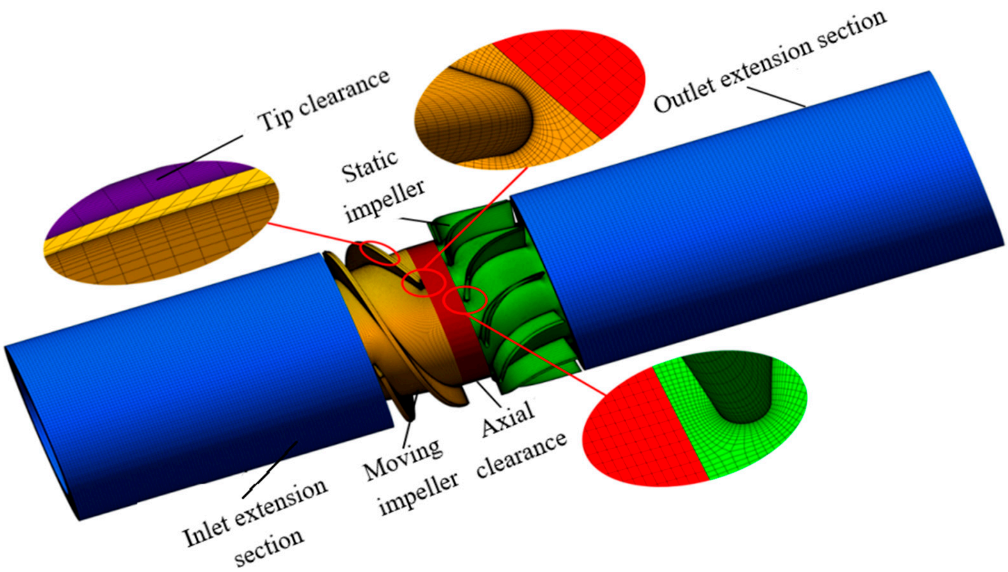

Figure 3. Grid system.

3.4. Numerical Simulation Setting

The inlet boundary condition is set as the velocity inlet boundary condition, and the velocity is calculated by the flow rate and cross-sectional area of the inlet pipe. The outlet boundary condition is a static pressure outlet boundary. The wall surface of the impeller wheel adopted the rotating coordinate wall surface, while the others remained stationary. The Frozen Rotor mode is used between rotatory and static parts while general connection, that is, direct connection, is used between static parts. Non-slip and non-penetration boundary conditions are used for all solid walls, and scalable wall function is used in the near wall area.

Pure water is selected as the working fluid medium to study the regular patterns of pressure load distribution on the helico-axial pump impeller blade surface. The density of water is 1000 kg/m^3, the kinematic viscosity is 1.01×10^{-6} m^2/s, and the compressibility has been neglected.

In this paper, CFX software is used to conduct the numerical simulation of the internal flow of the helico-axial pump. The SIMPLE method is used for solving pressure and velocity, and the calculation process is considered to be converged when the root-mean-square residual is below 10^{-5}.

3.5. Numerical Method Verification

In order to verify the reliability of the numerical calculation method adopted in this paper, the reliability of numerical calculation is verified by the experimental verification method. This experimental system platform can test the hydraulic performance of the helico-axial pump. In this study, the external characteristics test of a single pressurization unit of a pump is mainly carried out. In order to more easily capture the flow state in the impeller during the test, the diffuser and the pump body are made of transparent plexiglass, as shown in Figure 4.

(**a**) (**b**) (**c**)

Figure 4. Physical model of the helico-axial pump. (**a**) impeller (**b**) diffuser (**c**) pump body.

The helico-axial pump experimental platform consists of a frequency converter, torque meter, inlet and outlet throttle valve, inlet and outlet pressure sensor and electromagnetic flow meter, and so on, as shown in Figure 5. The precision of the main equipment is shown in Table 3. The accuracy of the above experiment equipment is reliable, and at the same time, the head and efficiency obtained in this way are also real and credible.

(**a**) (**b**)

Figure 5. Partial system configuration. (**a**) torque meter (**b**) experimental data acquisition system.

Table 3. The precision of main equipment.

Instrument	Range	Precision	Unit
Inlet pressure gauge	0–0.8	0.3 class	MPa
Outlet pressure gauge	0–1	±0.2%	MPa
Water flow meter	0–140	±0.5%	m^3/h
Torquemeter	0–50	0.2 class	N·m

To verify the reliability of the numerical methods, the numerical results are compared with the experimental results under the same operating conditions. Figure 6 shows the comparison of the experimental data and simulation results of head and efficiency, respectively. It can be seen that the change tendencies in the numerical results and the experimental results are consistent, and the relative error between each other are all within 5% in the flow rate range of 60~120 m^3/h. The comparison shows the results of the numerical simulations are reliable. The numerical simulation method used in this study has high reliability, and the calculation results can accurately predict the transport performance of the helico-axial pump.

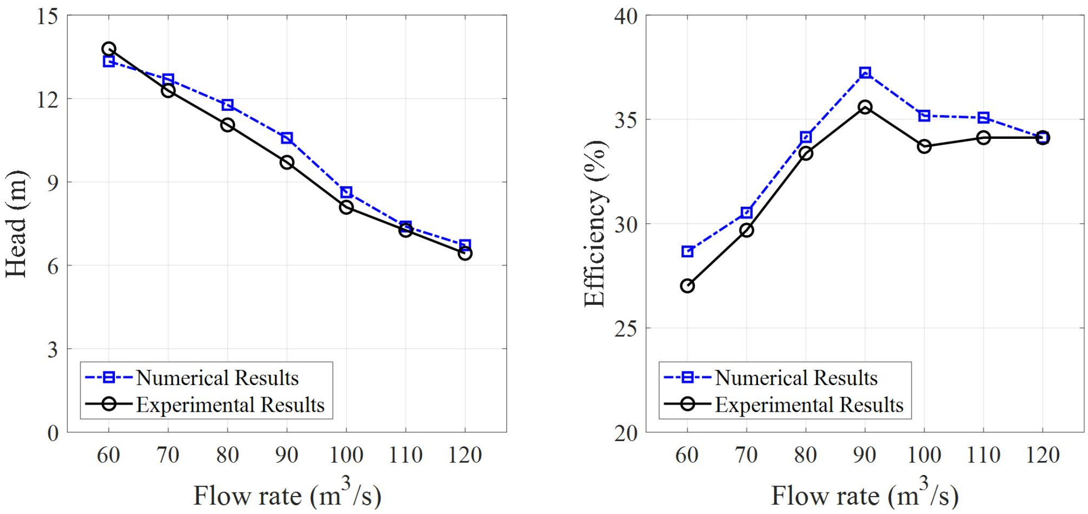

Figure 6. Comparison of experimental and numerical results.

4. Result Analysis

In the present work, five different flow rates, i.e., 80 m^3/h, 90 m^3/h, 100 m^3/h, 110 m^3/h and 120 m^3/h, were selected to study the regular patterns of blade surface load distribution on helico-axial pump impeller blade under different operation conditions. In the numerical simulations, the internal flow field of the helico-axial pump is seen as a three-dimensional steady flow field.

4.1. Static Pressure Distribution of Impeller Blade Surface under Different Flow Rates

In order to explore the work capacity of the helico-axial pump, the regular patterns of static pressure distribution of the helico-axial pump blade at different blade heights under different flow rates are studied. In this paper, three streamlines on the blade surface are selected for analysis, which is span = 0 (intersected line of blade and hub), 0.5 (middle streamline) and 1 (streamline at blade rim), which are shown in Figure 7.

The static pressure data of the three streamlines under each working condition is extracted, respectively. The relative positions of static pressure data points on each streamline are conducted with normalization processing. The position where the relative position of the blade is 0 means the impeller blade inlet, and the position where the relative position of the blade is 1 means the impeller blade outlet. The static pressure distribution of the helico-axial pump blade surface is finally obtained, as shown in Figure 8.

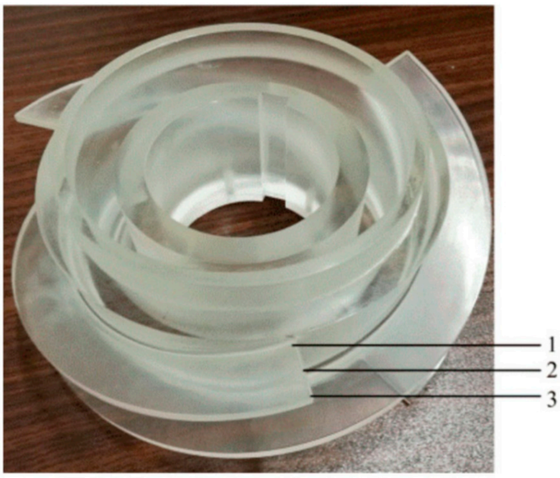

1. Hub streamline, span = 0.0

2. Middle streamline, span = 0.5

3. Rim streamline, span = 1.0

Figure 7. Streamlines on the blade surface.

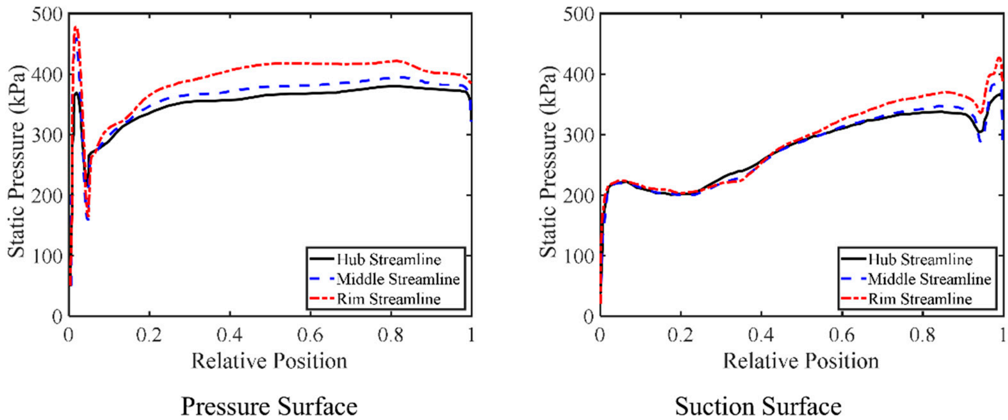

(**a**)

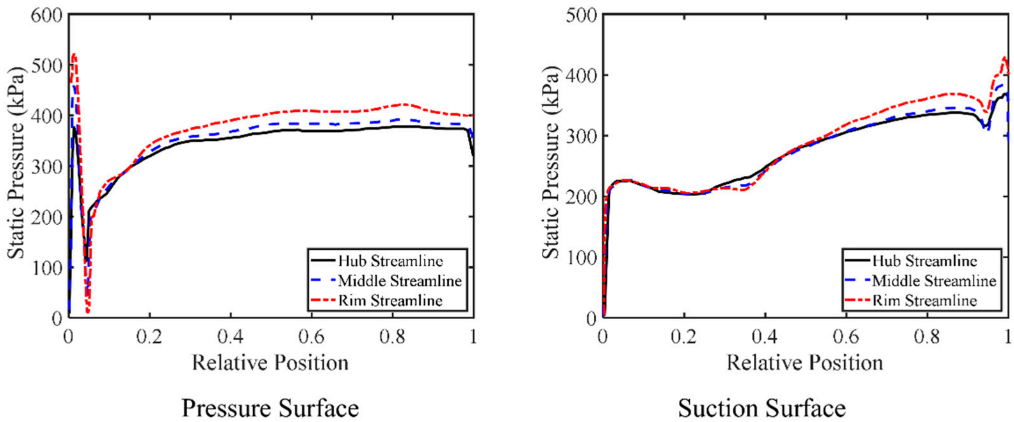

(**b**)

Figure 8. *Cont.*

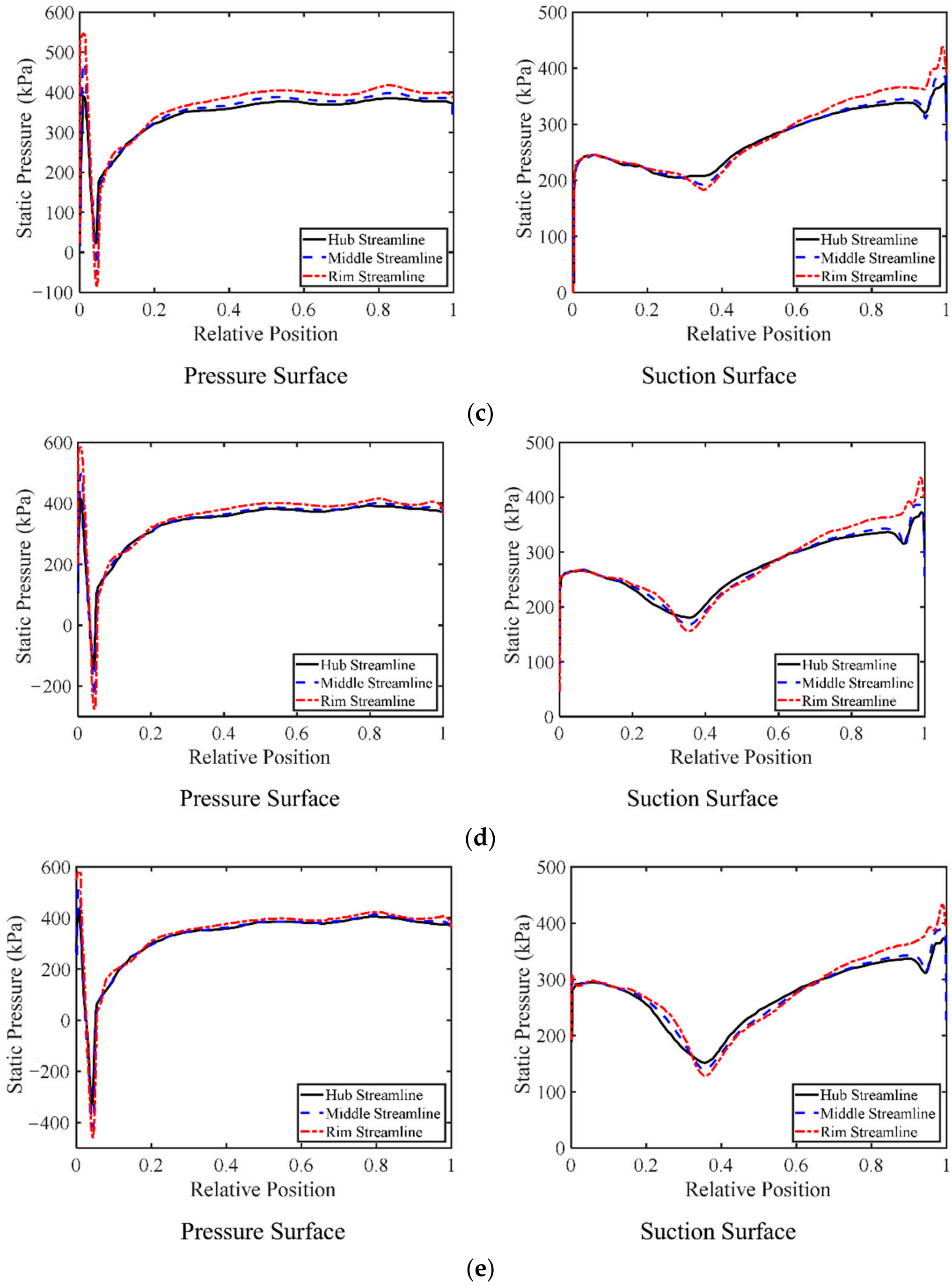

Figure 8. Static pressure distribution curves of helicon-axial pump with different flow rates. (**a**) Q = 80 m^3/h (**b**) Q = 90 m^3/h (**c**) Q = 100 m^3/h (**d**) Q = 110 m^3/h (**e**) Q = 120 m^3/h.

It can be known from comparing the static pressure distribution curves on the blade surface in Figure 8a–e that, under each flow rate, the variation patterns of the static pressure of each streamline on the blade working surface and back surface are similar. The static pressure value of the working surface increases gradually from hub to rim, while the static pressure value of the back surface alternatively changes from hub to rim, showing uneven static pressure distribution on the blade surface. It can also be seen from Figure 8 that, compared with the working condition of large flow rate conditions, under the working condition of small flow rate, the static pressure difference between each streamline of the helico-axial pump working face is obviously larger, indicating that the static pressure gradient of the working surface of helico-axial pump impeller blade gradually decreases with the increase of flow rate in the direction of blade height. The static pressure fluctuation in the inlet area also gradually increases, indicating that with the increase in flow rate, the energy loss of the impeller inlet area gradually increases, which is consistent with the gradual decrease of impeller hydraulic efficiency with the increase of flow in the external characteristic of helico-axial pump. It can also be seen from Figure 8 that, with the increase in flow rate, the lowest point of static pressure at different blade heights on the back surface of the helico-axial pump blade gradually transfers from the relative position of 0.2 to 0.4, and the low-pressure area gradually increases, indicating that, with the increase of flow rate, the low-pressure area gradually expands when helico-axial pump blade back surface is in the relative position of 0.2~0.4.

4.2. Pressure Load Distribution of Impeller Blade under Different Flow Rate

The difference between the static pressure on the blade working surface and the back surface of the helico-axial pump is used to obtain the pressure load distribution of the impeller blade from the inlet to the outlet, as shown in Figure 9. It can be seen from Figure 9 that, under the working conditions of different flow rates, all the pressure load distribution curves of the helico-axial pump impeller blade surface at different blade heights show a trend of increasing first and decreasing then, indicating that the work capacity of helico-axial pump impeller from inlet to outlet increases first and decreases then. It can also be seen from Figure 9 that in the impeller inlet area, with the increase of flow rate, the range of negative blade pressure load in this area increases gradually, indicating that, with the increase of flow rate, the highly efficient work capacity area of impeller domain starts to narrow while the negative work capacity area of impeller inlet gradually expands.

It also can be seen from Figure 9a,b that, under the working condition of a small flow rate, within the range of relative position from 0 to 0.2, the pressure load of the hub streamline reaches the maximum, and the difference between the pressure load values of the middle streamline and the rim streamline are very small. Meanwhile, within the range of relative position of from 0.2 to 1, the pressure load at the rim streamline is the largest, followed by that of the middle streamline, and that of the hub is the minimum, indicating that, under the working condition of small flow rate, the work capacity of the hub within the range of relative position of 0~0.2 is obviously stronger than that of other areas of the impeller and the work capacity from hub to rim within the range of relative position of 0.2~1 gradually increases. With the increase of flow rate, under the working conditions of the designed flow rate and large flow rate, the area with a strong work capacity of the hub gradually expands while the area with a strong work capacity of the rim gradually narrows. Additionally, it can also be seen from Figure 9 that, with the increase in flow rate, the fluctuation of pressure load curves of each streamline gradually increases, and its peak value gradually deviates towards the outlet. It can be known from the literature [4] that the blade load distribution is relative to the relative velocity. The fluctuation of load curves will lead to fluctuation of relative velocity inside the impeller and the flow inside the impeller becomes more turbulent. Contrarily, the more uniform the velocity distribution inside the impeller, the more stable the internal flow. The maximum load value of the blade shall be optimal in the middle of the impeller with a slight inclination to the inlet. As the maximum load moves to the outlet, pump performance begins to degrade.

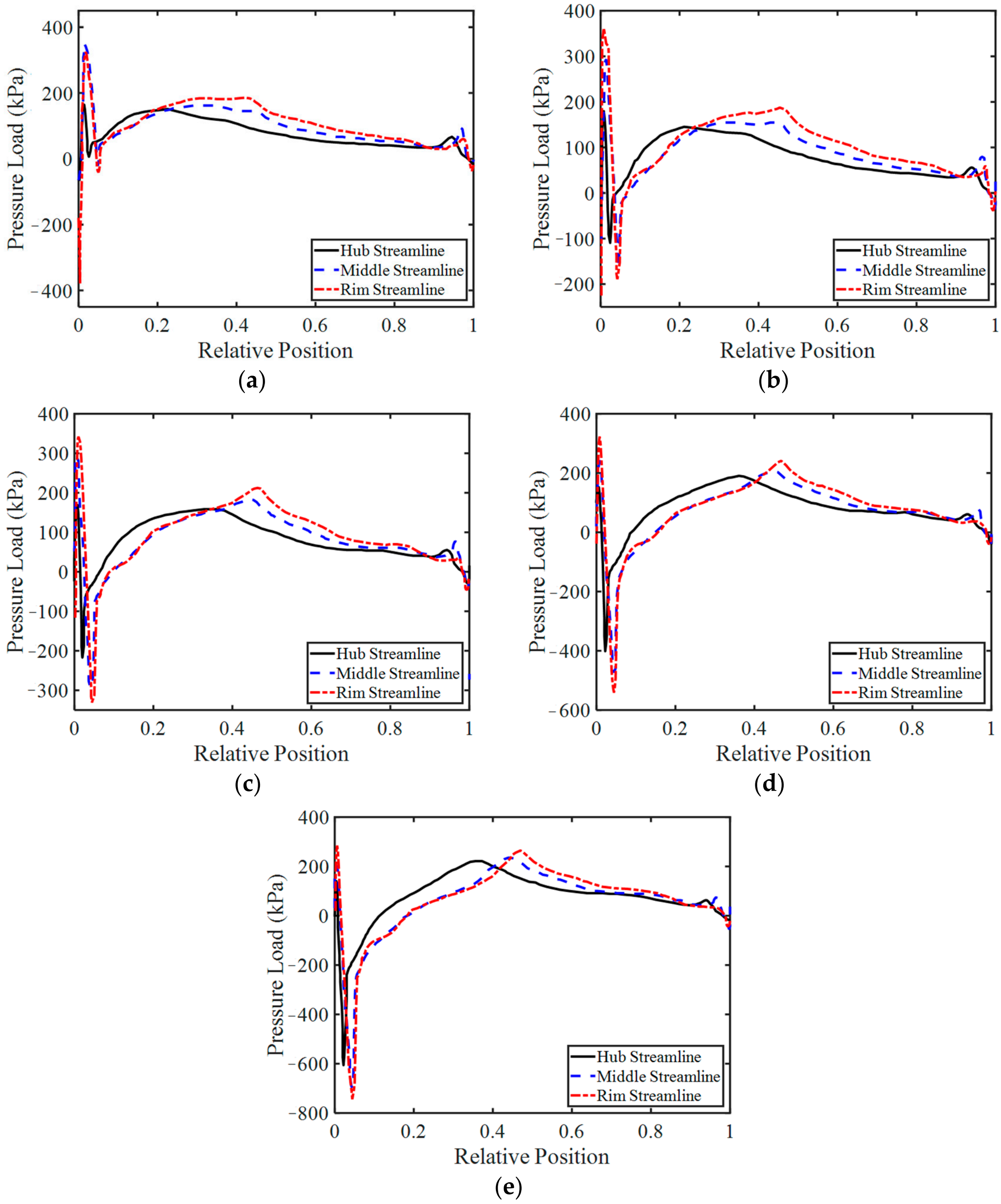

Figure 9. Pressure load distribution curves of helico-axial pump with different flow rates. (**a**) $Q = 80\ m^3/h$ (**b**) $Q = 90\ m^3/h$ (**c**) $Q = 100\ m^3/h$ (**d**) $Q = 100\ m^3/h$ (**e**) $Q = 120\ m^3/h$.

5. Conclusions

To obtain the effect of flow rate on regular patterns of pressure load distribution on helico-axial pump impeller blade surface, a numerical study of the helico-axial pump under different flow rates has been carried out, and the following conclusions are obtained:

(1) With the increase of flow rate, the head of both the helico-axial pump and impeller gradually decreases, while the hydraulic efficiency of the helico-axial pump increases first and decreases then with a gradual lowering of impeller efficiency. Moreover, with the increase in flow rate, the decreased rate of the impeller hydraulic efficiency under the working condition of a large flow rate is apparently higher than that under the working condition of a small flow rate.

(2) The static pressure difference between each streamline of the helico-axial pump impeller working surface under the working condition of a small flow rate is significantly

larger than that under the working condition of a large flow rate. With the increase in flow rate, the lowest point of static pressure on the back surface of the helico-axial pump blade at different blade heights gradually shifts from the relative position of 0.2 to 0.4, and the low-pressure area gradually expands.

(3) Under different flow rates, the pressure load distribution curves of the impeller blade surface at different blade heights all show the trend of increasing first and decreasing then. In the impeller inlet area, with the increase in flow rate, the range of negative blade pressure load in the area gradually expands. Under the working condition of a small flow rate, the work capacity of the hub is significantly stronger than other areas of the impeller within the range of relative position of 0~0.2, and the work capacity gradually increases from hub to rim within the range of relative position of 0.2~1. With the increase in flow rate, the area of the strong work capacity of the hub gradually expands while the area of the strong work capacity of the rim gradually narrows.

Author Contributions: Conceptualization, Z.H. and G.S.; methodology, Z.H.; software, Z.H., G.S. and H.W.; writing—original draft preparation, Z.H. and H.W.; writing—review and editing, G.S.; supervision, G.S. All authors have read and agreed to the published version of the manuscript.

Funding: This work was supported by the Central Leading Place Scientific and Technological Development Funds for Surface Project (2021ZYD0038); Open Research Fund Program of State Key Laboratory of Hydroscience and Engineering (sklhse-2021-E-03); The National Key Research and Development Program (2018YFB0905200); The Key scientific research fund of Xihua University of China (Grant No. Z1510417); The Open Research Subject of Key Laboratory of Fluid and Power Machinery (Xihua University), Ministry of Education (grant number szjj2014-045).

Institutional Review Board Statement: Not applicable.

Informed Consent Statement: Not applicable.

Data Availability Statement: Not applicable.

Conflicts of Interest: The authors declare no conflict of interest.

References

1. Saadawi, H. An overview of multiphase pumping technology and its potential application for oil fields in the gulf region. In Proceedings of the International Petroleum Technology Conference, Dubai, United Arab Emirates, 4–6 December 2007.
2. Falcimaigne, J.; Brac, J.; Charron, Y.; Pagnier, P.; Vilaginès, R. Multiphase Pumping: Achievements and Perspectives. *Oil Gas Sci. Technol.* **2002**, *57*, 99–107. [CrossRef]
3. Ming, L.; Lei, T.; Shuliang, C. Method of dynamic mode decomposition and reconstruction with application to a three-stage multiphase pump. *Energy* **2020**, *208*, 1118343.
4. Kim, J.H.; Lee, H.C.; Kim, J.H.; Choi, Y.S.; Yoon, J.Y.; Yoo, I.S.; Choi, W.C. Improvement of Hydrodynamic Performance of a Multiphase Pump Using Design of Experiment Techniques. *J. Fluids Eng.* **2015**, *137*, 081301. [CrossRef]
5. Wang, J.; Zha, H.; McDonough, J.; Zhang, D. Analysis and numerical simulation of a novel gas–liquid multiphase scroll pump. *Int. J. Heat Mass Transf.* **2015**, *91*, 27–36. [CrossRef]
6. Shi, Y.; Zhu, H.; Zhang, J.; Zhang, J.; Zhang, J. Experiment and numerical study of a new generation three-stage multiphase pump. *J. Pet. Sci. Eng.* **2018**, *169*, 471–484. [CrossRef]
7. Zhang, J.; Zhu, H.; Yang, C.; Li, Y.; Wei, H. Multi-objective shape optimization of helico-axial multiphase pump impeller based on NSGA-II and ANN. *Energy Convers. Manag.* **2011**, *52*, 538–546. [CrossRef]
8. Suh, J.W.; Kim, J.H.; Choi, Y.S.; Joo, W.G.; Lee, K.Y. A study on numerical optimization and performance verification of multiphase pump for offshore plant. *Proc. Inst. Mech. Eng. Part A J. Power Energy* **2017**, *231*, 382–397. [CrossRef]
9. Shi, G.; Liu, Z.; Xiao, Y.; Yang, H.; Li, H.; Liu, X. Effect of the inlet gas void fraction on the tip leakage vortex in a multiphase pump. *Renew. Energy* **2020**, *150*, 46–57. [CrossRef]
10. Liu, M.; Tan, L.; Xu, Y.; Cao, S. Optimization design method of multi-stage multiphase pump based on Oseen vortex. *J. Pet. Sci. Eng.* **2019**, *184*, 106532. [CrossRef]
11. Kim, S.; Kim, Y.I.; Kim, J.H.; Choi, Y.S. Three-objective optimization of a mixed-flow pump impeller for improved suction performance and efficiency. *Adv. Mech. Eng.* **2020**, *11*, 7–40. [CrossRef]
12. Xu, Y.; Cao, S.; Sano, T.; Wakai, T.; Reclari, M. Experimental Investigation on Transient Pressure Characteristics in a Helico-Axial Multiphase Pump. *Energies* **2019**, *12*, 461. [CrossRef]

13. Zhang, J.; Cai, S.; Zhu, H.; Zhang, Y. Experimental investigation of the flow at the entrance of a rotodynamic multiphase pump by visualization. *J. Pet. Sci. Eng.* **2015**, *126*, 254–261. [CrossRef]
14. Zhang, J.; Cai, S.; Li, Y.; Zhu, H.; Zhang, Y. Visualization Study of Gas-Liquid Two-Phase Flow Patterns inside a Three-Stage Rotodynamic Multiphase Pump. *Exp. Therm. Fluid Sci.* **2016**, *70*, 125–138. [CrossRef]
15. Liu, M.; Tan, L.; Cao, S. Design method of controllable blade angle and orthogonal optimization of pressure rise for a multiphase pump. *Energies* **2018**, *11*, 1048. [CrossRef]
16. Zhang, J.-X.; Zhang, J.-Y.; Zhou, Y.; Cheng, Z.-Y.-Y.; Cap, G.-D. Investigation on the performance of a helico-axial multiphase pump under slug flow. *Pet. Sci.* **2022**, *19*, 1812–1824. [CrossRef]
17. Suh, J.W.; Kim, J.W.; Choi, Y.S.; Kim, J.Y.; Joo, W.G.; Lee, K.Y. Development of numerical Eulerian-Eulerian models for simulating multiphase pumps. *J. Pet. Sci. Eng.* **2018**, *162*, 588–601. [CrossRef]
18. Cao, F.; Gao, T.; Li, S.; Xing, Z.; Shu, P. Experimental analysis of pressure distribution in a twin screw compressor for multiphase duties. *Exp. Therm. Fluid Sci.* **2011**, *35*, 219–225. [CrossRef]
19. Xiao, Y.; Gui, Z.; Li, X.; Shu, Z.; Shi, G.; Gu, C. Numerical Investigation of Gas-Liquid Flow in a Multiphase Pump with Special Emphasis on the Effect of Tip Leakage Vortex on the Gas Flow Pattern. *J. Mar. Sci. Eng.* **2022**, *10*, 1665. [CrossRef]
20. Yu, Z.; Zhu, B.; Cao, S. Interphase force analysis for air-water bubbly flow in a multiphase rotodynamic pump. *Eng. Comput.* **2015**, *32*, 2166–2180. [CrossRef]
21. Cao, S.; Peng, G.; Yu, Z. Hydrodynamic Design of Rotodynamic Pump Impeller for Multiphase Pumping by Combined Approach of Inverse Design and CFD Analysis. *J. Fluids Eng.-Trans. ASME* **2005**, *127*, 330–338. [CrossRef]
22. Quan, H.; Li, Y.; Kang, L.; Yu, X.; Song, K.; Wu, Y. Influence of Blade Type on the Flow Structure of a Vortex Pump for Solid-Liquid Two-Phase Flow. *Machines* **2021**, *9*, 353. [CrossRef]
23. Li, D.; Zhu, Y.; Lin, S.; Gong, R.; Wang, H.; Luo, X. Cavitation effects on pressure fluctuation in pump-turbine hump region. *J. Energy Storage* **2022**, *47*, 103936. [CrossRef]
24. Li, X.; Gao, P.; Zhu, Z.; Li, Y. Effect of the blade loading distribution on hydrodynamic performance of a centrifugal pump with cylindrical blades. *J. Mech. Sci. Technol.* **2018**, *32*, 1161–1170. [CrossRef]
25. Shi, G.; Yan, D.; Liu, X.; Xiao, Y.; Shu, Z. Effect of the Gas Volume Fraction on the Pressure Load of the Multiphase Pump Blade. *Processes* **2021**, *9*, 650. [CrossRef]
26. Zhang, M.; Tsukamoto, H. Unsteady Hydrodynamic Forces due to Rotor-Stator Interaction on a Diffuser Pump with Identical Number of Vanes on the Impeller and Diffuser. *J. Fluids Eng.-Trans. ASME* **2005**, *127*, 743–751. [CrossRef]
27. Zhou, L.; Shi, W.; Wei, L.; Agarwal, R. Numerical and Experimental Study of Axial Force and Hydraulic Performance in a Deep-Well Centrifugal Pump with Different Impeller Rear Shroud Radius. *J. Fluids Eng.-Trans. ASME* **2013**, *135*, 104501. [CrossRef]
28. Li, J.W.; Zhang, Y.N.; Liu, K.H.; Xian, H.Z.; Yu, J.X. Numerical simulation of hydraulic force on the impeller of reversible pump turbines in generating mode. *J. Hydrodyn.* **2017**, *29*, 603–609. [CrossRef]
29. Zhu, D.; Xiao, R.; Liu, W. Influence of leading-edge cavitation on impeller blade axial force in the pump mode of reversible pump-turbine. *Renew. Energy* **2021**, *163*, 939–949. [CrossRef]
30. Kang, C.; Zhu, Y.; Li, Q. Effects of hydraulic loads and structure on operational stability of the rotor of a molten-salt pump. *Eng. Fail. Anal.* **2020**, *117*, 104821. [CrossRef]
31. Zhou, W.; Wang, Y.; Li, C.; Zhang, W.; Wu, G. Analysis of fluid-induced force of centrifugal pump impeller with compound whirl. *Alex. Eng. J.* **2021**, *59*, 4247–4255. [CrossRef]
32. Shi, G.; Zhu, Z.; Wang, B.; Wen, H. Effect of the Gap Matching Relation on the Pressure Pulsation Characteristics at Blade's Surface of the Multiphase Pump. *Machines* **2022**, *10*, 418. [CrossRef]
33. Liu, M.; Tan, L.; Cao, S. Theoretical model of energy performance prediction and BEP determination for centrifugal pump as turbine. *Energy* **2019**, *172*, 712–732. [CrossRef]
34. Wilcox, D.C. *Turbulence Modeling for CFD*; DCW Industries: La Canada, CA, USA, 1998.
35. Menter, F.R. Two-equation eddy-viscosity turbulence models for engineering applications. *AIAA J.* **1994**, *32*, 1598–1605. [CrossRef]